Highly efficient spin qubit to photon interface assisted by a photonic crystal cavity

K. Wu*[a], T. Descamps[b], B. Marzban[a], J. C. Müller[b], S. Kindel[b], M. Künne[b], F. Merget[a], H. Bluhm[b] and J. Witzens[a]
[a]Institute of Integrated Photonics, RWTH Aachen University, Aachen, 52074, Germany
[b]Quantum Technology Group, 2nd Institute of Physics, RWTH Aachen University, Aachen, 52074, Germany

ABSTRACT

Interfacing semiconductor with photonic qubits plays an important role in quantum networks. We model a photon to spin qubit interface based on an optically active gate-defined quantum dot embedded in a two-dimensional photonic crystal cavity constraining its emission profile with a low enough quality factor for emission wavelength tuning. By matching the cavity-mode k-vector and reciprocal lattice of the crystal, vertical emission is obtained. A reflector below the cavity increases not only the light extraction efficiency, but also tailors the extracted beam profile to match that of a single mode fiber, into which photons emitted by the quantum dot are coupled with a probability above 50%. The efficiency is primarily limited by metal electrode absorption. In addition to trapping the exciton, the electrode system embedded inside the cavity allows trapping, manipulation and readout of a pair of electrons encoding a spin qubit in a singlet-triplet configuration, whose quantum state can be transferred to and from the exciton by utilizing an existing protocol. Experimental realization of these devices is currently in progress with first results in regard to fabrication also reported.

Keywords: quantum computing, optical interface, spin qubit, photonic crystal cavity, gate-defined quantum dot.

1. INTRODUCTION

Semiconductor-based quantum dot systems are promising candidates for future quantum computation and information systems. Compared to isolated atomic qubits such as trapped ions, semiconductor qubit devices have the advantage of being compatible with large-scale integration on a semiconductor chip utilizing standard fabrication techniques. One example of such a semiconductor system is a gate defined quantum dot (GDQD), which is defined by applying an electrostatic potential with surface metal gates to a two-dimensional (2D) electron gas to confine single electrons in tunable energy minima. Researchers have shown that all the quantum computing prerequisites are satisfied for GaAs GDQD qubits, such as qubit initialization, readout [1] and coherent control [2, 3].

Coherent and efficient interfacing between stationary spin qubits and photonic qubits remains a big challenge in order to realize quantum networks suitable for long-distance quantum communication and distributed quantum computation. Preliminary works in this direction have shown photoelectron trapping and interaction with a GDQD [4, 5]. However, the lack of hole confinement in conventional heterostructures used for GDQD prevents the coherent coupling between the electron spin state and the photon due to the lost information of the hole spin. To remediate this inherent limitation, various schemes have been proposed such as g-factor engineering [6, 7] to eliminate the entanglement between the photo-generated electron and hole. Another approach is the integration of an optically active quantum dot which is able to trap excitons, and thus both the photogenerated electron and hole, as an intermediary between the photonic qubit and the GDQD spin qubit. Following this path, a protocol has been developed to transfer the quantum state of an exciton trapped in an InGaAs self-assembled quantum dot (SAQD) to a singlet-triplet GDQD by tunneling-based coupling of the photogenerated electron [8]. However, without further optical engineering, the probability in such devices of capturing a photon or of emitting one into a fiber is only about 2% due to total internal reflection (TIR) at the chip surface [9], which severally limits the efficiency of the spin-photon interface.

kwu@iph.rwth-aachen.de; phone +49 241 80 20020; iph.rwth-aachen.de

Physics and Simulation of Optoelectronic Devices XXX, edited by B. Witzigmann, M. Osiński, Y. Arakawa, Proc. of SPIE Vol. 11995, 1199507 © The Authors. Published under a Creative Commons Attribution CC-BY 3.0 License · doi: 10.1117/12.2614665

In order to improve optical interfacing to SAQDs, 3D-microstructures such as micropillar cavities [10], nanowires [11], or micro-lenses [12, 13] have been investigated. Although the efficiency with which emitted photons can be collected has been boosted up to 66% by etching a micropillar cavity with a carefully selected SAQD located in its center [10], scalable quantum circuits based on such structures remain a big challenge, since the position and emission spectrum of SAQDs are difficult to control [14]. Besides, etching of the micropillar cavity separates the SAQD from other on-chip devices and thus makes connectivity with a chip-scale computing system very difficult, even at a conceptual level.

A gate defined optically active quantum dot (OAQD) is another option for an exciton trap that can be integrated in the quantum-state transfer protocol [8]. The OAQD is defined by patterning metal electrodes on both sides of a quantum well (QW) whose band edge energies are locally modified by the electric field created by the electrodes (in this case confining the hole, see below). As a result of the quantum-confined Stark effect (QCSE), the energy of excitons is also locally reduced, so that a complete electron/hole pair can be trapped. OAQDs have several advantages over SAQDs for the envisioned platform. For one, OAQDs can be deterministically fabricated next to the GDQD by top-down fabrication processes. On the other hand, SAQDs are randomly distributed and need to be located and carefully selected before patterning the GDQD. Moreover, the exciton emission and absorption wavelength can be tuned by changing the voltage difference between the trap gates [15].

Photonic crystal cavities (PCC) defined in a 2D planar photonic crystal can be used to enhance photon absorption by and emission from two-level quantum systems by utilizing the Purcell effect [16], or to adjust the far field emission pattern by utilizing the band-folding technique [17, 18]. The combination of PCCs with SAQDs to enhance the photon-exciton coupling has been widely studied [19]. On the other hand, the integration of OAQDs and PCCs has only recently started to attract more attention. A recent study reports the cavity enhanced photoluminescence of a QW embedded in a PCC with an OAQD defined by electrodes deposited on the surface of the semiconductor-air interface [20]. We have proposed PCC enhanced photon extraction from an OAQD embedded in a carefully designed photonic crystal H4 cavity [21], with a device modeled to have a photon extraction efficiency of 55.8% in an almost ideal Gaussian-shaped far field pattern (overlap > 95%). However, a complete device integrating a coupled GDQD spin qubit and an OAQD in a PCC has not yet been studied.

In this paper, we propose a novel optical interface between a free space photonic qubit and a singlet-triplet spin qubit stored in a GDQD. We use an OAQD as an exciton trap, which is located in the center of a carefully designed photonic crystal H4 cavity. The GDQD, OAQD and the photonic crystal cavity are defined in a 220 nm thick GaAs/AlGaAs hetero-structure membrane. The cavity is designed in such a way that highly efficient vertical emission is achieved at the working wavelength of the OAQD (823 nm). A metal back-reflector is assumed to be deposited on the silicon substrate onto which the GaAs/AlGaAs stack is transferred [21] and serves to coherently recycle photons that are emitted downwards, comparable to what is commonly done in grating couplers [22, 23]. Moreover, the far field emission pattern can be optimized by adjusting the position of the back-reflector by selecting in k-space which field components of the PCC mode are preferentially extracted [21]. According to our numerical calculations, this structure achieves a power extraction efficiency over 50% if collection optics with a numerical aperture (NA) greater than 0.6 is used. The far field emission pattern has a 98.3% overlap with an ideal Gaussian beam, which is ideal for coupling into a single mode fiber.

This paper is organized as follows. In Section 2, we introduce the detailed design, including the GaAs/AlGaAs hetero-structure, the GDQD, the OAQD, the photonic crystal cavity and their integration. Optical simulation results will be presented in Section 3. Experimental progress including scanning electron micrograph (SEM) images of our first fabricated test sample is described in Section 4. Finally, a conclusion and an outlook will be given in Section 5.

2. STRUCTURE DESCRIPTION AND MODELING

Fig. 1(a) gives a schematic overview of the presented structure. The 220 nm free-standing GaAs/AlGaAs heterostructure consists of a 20 nm GaAs QW sandwiched in between two 90 nm $Al_{0.33}Ga_{0.67}As$ barrier layers and two 10 nm GaAs cap layers (Fig. 1(b)). A Ti/Au electrode system is deposited on both sides of the membrane to define the GDQD and OAQD. Moreover, a photonic crystal cavity is patterned in the membrane with its center coinciding with the OAQD. Finally, in the simulations a bottom reflector is assumed to be located below the membrane (not shown) to recycle photons that are emitted downwards, at a judiciously chosen distance to maximize extraction efficiencies and to obtain the targeted Gaussian emission pattern. For simplicity, the membrane is assumed to be surrounded by vacuum on both sides here, even though in a realistic fabrication scenario a polymer might be located between the membrane and the bottom reflector onto which it is mounted. While this can have some impact on the device performance in the order of a few additional percents

drop in extraction efficiency [21], we expect to maintain a collection efficiency above 50% even then if a sufficiently wide NA is used. The device is described in more detail in the following.

The detailed geometry of the GDQD and OAQD electrode layout, on the top side of the GaAs/AlGaAs membrane, is depicted in Fig. 1(c). The electrodes are made of Au/Ti nanowires with a thickness of 9 nm (2 nm Ti and 7 nm Au) and a width of 30 nm. To ensure independent voltage control, adjacent wires are separated from each other by a distance of 50 nm. They create local potential minima in the two-dimensional electron gas (2DEG) in the GaAs QW. As a result, we create a double quantum dot which is able to host 2 electrons, upon which the singlet-triplet spin qubit can be defined and manipulated.

The OAQD consists of a round trap gate with a radius of 50 nm surrounded by five finger-shaped guard gates (Fig. 1(c)). The left two guard gates, which are shared between the GDQD and OAQD, are used to adjust the tunnel barrier height between the GDQD and the OAQD. The negative voltage difference between the trap and guard gates, $\Delta V = V_T - V_G < 0$, ensures that the photoexcited hole is electrostatically trapped under the trap gate (Fig. 1(b)). The pairing electron is confined laterally by the Coulomb interaction with the hole [15] and the overall photogenerated exciton confined by mean of the QCSE. By changing the electric field between the trap gates on both sides of the layer stack, the emission and absorption wavelength associated to the exciton can be tuned around 823 nm at cryogenic temperature, which is the designed working wavelength for which the surrounding photonic crystal has been optimized. In contrast to the GDQD, which is defined by metal gates on the top surface of the GaAs membrane only, the OAQD requires symmetric gates on both sides of the membrane in order to ensure a strongly localized electric field and independent tuning of the exciton trap [15].

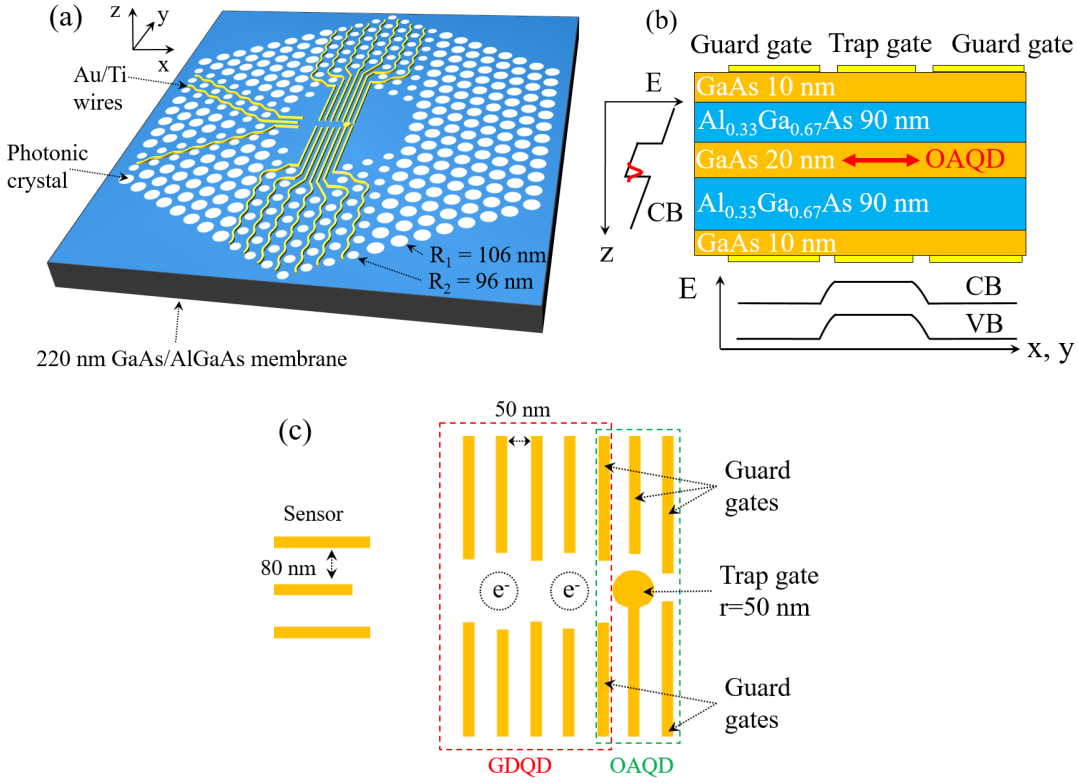

Figure 1. (a) Overview of the photonic crystal cavity and electrode system. Part of the etched air holes has a smaller radius than nominal to facilitate routing the metal wires through the photonic crystal. A bottom mirror can be placed below the membrane to further increase the power extraction efficiency and adjust the shape of the far field pattern. (b) GaAs/AlGaAs layer stack structure. The band-edge energies of the conduction (CB) and valence band (VB) are shown as a function of spatial coordinates. (c) Top view of the GDQD, the OAQD, and the readout sensor. The OAQD electrodes are patterned on both sides of the membrane, while the GDQD and the sensor only require top side electrodes. All wires have a width of 30 nm and a thickness of 9 nm (2 nm Ti and 7 nm Au).

By partially n-doping AlGaAs layers inside the stack, the 2DEG can be populated outside of the quantum dots without the need of applying an external voltage to reach the accumulation condition. However, to observe the Stark shift, the QW must then be locally depleted as the large electron density of the 2DEG would otherwise screen the external electric field applied by the trap gates. The guard gates can then be used for depletion while the central trap gates can be anti-symmetrically biased to create an electric field, while keeping the electrostatic potential at the center of the QW at zero.

A quantum dot charge sensor is defined by three horizontal metal gates (Fig. 1(c)). By utilizing the Pauli spin blockade together with charge sensing [24-26], the sensor is able to detect the singlet-triplet spin state of the trapped electron pair in the double quantum dot. When the two trapped electrons are in a singlet spin state, the electron in the left quantum dot can tunnel to the right quantum dot (or vice versa) as a result of electrode voltage tuning. However, this procedure is not possible in the case of a triplet spin state due to the Pauli exclusion principle. Due to the different spatial charge distribution in these two cases, the resistance changes in the sensing area between the sensor electrodes and the double quantum dot, which can be measured by an RF-reflectometry measurement [27].

A 2D photonic crystal is patterned as a triangular lattice of air holes fully etched through the 220 nm thick membrane with a lattice constant a = 282 nm and a hole radius R_1=106 nm. A PCC is defined by a modified hexagonal H4 cavity with a side length of 4a centered on the OAQD. As indicated in Fig. 1(a), several holes are left out on the top, bottom and left side of the H4 cavity in order to facilitate routing of the metal wires through the photonic crystal lattice.

The functionality of our structure is not affected by the broken six-fold symmetry of the H4 cavity caused by these modifications. The transfer protocol between the photonic qubit and singlet-triplet spin qubit has been chosen such that only one cavity mode – here the y-polarized one – plays a role [8], with the photonic qubit based on frequency rather than polarization entanglement. It uses a static in-plane magnetic field (Voigt configuration) oriented along the x-direction and setting the axis of quantization of the spins. Degeneracy between x- and y-polarized cavity modes is thus no longer required. As a tradeoff, the cavity mode's quality (Q-)factor needs to be low enough to support both optical frequencies. This requirement is fulfilled while maintaining the targeted beam forming and light extraction efficiency, as shown in the next section. As a consequence of the light's y-polarization, the utilized cavity dipole mode is analogous to a Fabry-Perot resonance propagating along the x-direction (Fig. 2(c)), so that the bottom- and topside modifications of the cavity have a minimal impact. The wires have also been routed in a way to minimize the overlap with the E-field of the cavity mode, so as to reduce losses from electrode absorption. In order to relax the overlay tolerance of the wire deposition process, the radius of air holes along the wire paths is also reduced from R_1 = 106 nm to a minimum of R_2 = 96 nm. Despite all these modifications, the cavity continues to support confined transverse electric (TE) modes in a wide wavelength range reaching from 780 nm to 1030 nm (defining the photonic crystal's effective bandgap), including the required dipole mode at the 823 nm OAQD emission wavelength. Due to the relatively large cavity size, the nearest hole is located ~1 µm from the OAQD and ~600 nm from the outer GDQD electron. These minimum distances were taken as design requirements in order to reduce the electrostatic interaction with traps created by defects at the etched interfaces.

A reflector is placed beneath the layer stack to recycle the downward propagating light. Moreover, the far-field emission pattern of the OAQD can be modified by adjusting the distance between the OAQD and the reflector, due to selective constructive interference between the upwards emitted and redirected beams for selected in-plane k-vectors [21]. A Gaussian-like far field pattern is obtained when the constructive interference condition is satisfied for in-plane k-vectors equal to 0.

In a QW, the energy degeneracy between the heavy and light holes is lifted due to their different effective masses, with heavy holes presenting the lowest energy. As a result, the exciton with the lowest energy consists of an electron and a heavy hole, which interacts preferentially with the TE electromagnetic field. For the reasons explained above arising from the transfer protocol, we further model the OAQD emission by a dipole orientated in the y-direction only.

3. SIMULATION RESULTS AND ANALYSIS

The modeling is performed using Lumerical's FDTD package. The membrane stands free in vacuum. A perfect mirror is realized by setting the boundary condition in the negative z-direction to a perfect metal, whereas other boundary conditions are set as perfectly matched layers (PML). The emitted field is obtained by applying a far field transform to the field recorded by a probe parallel to and 10 nm above the surface of the slab. This yields information on the far field pattern as well as on the extraction efficiency, that is calculated as $\eta_{tot}(NA) = P_{out}(NA)/P_{dip}$, where $P_{out}(NA)$ and P_{dip} are the power emitted out of the cavity within a numerical aperture NA and out of the dipole, respectively. P_{dip} is recorded by a monitor box formed by six 2D power monitors surrounding the dipole inside the GaAs quantum well. Since GaAs is

transparent at 823 nm at cryogenic temperatures (4 K) and there is no other absorptive material inside the monitor box (the metal wires are outside), this is an adequate measurement of the radiated dipole power. An additional monitor placed 60 nm below the top surface of the membrane serves to record the cavity mode profiles.

Figure 2(a) shows the recorded cavity power spectrum from 790 nm to 850 nm, obtained from a cavity ring down simulation after excitation by a y-orientated TE dipole located in the center of the cavity. Since this frequency range lies within the TE bandgap (780 nm to 1030 nm), we observe several cavity modes, two of which are highlighted by a red and green circle at 816 nm and 823 nm, respectively. The peak at 816 nm has the highest power and the highest quality factor (Q-factor), while the mode at 823 nm is the utilized cavity mode. The lattice constant of the photonic crystal is optimized in such a way that the working wavelength range of the OAQD falls within this resonance. Figures 2(b) and 2(c) display the $|H_z|$ field component inside the cavity for the 816 nm and 823 nm modes, respectively.

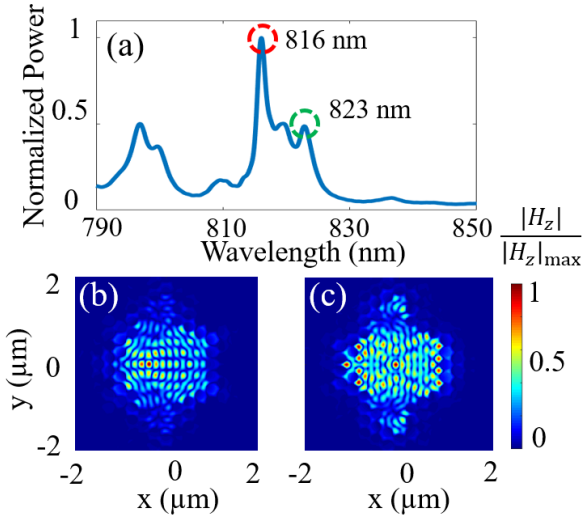

Figure 2. Real space field of the photonic crystal cavity modes. (a) Normalized cavity power spectrum from 790 nm to 850 nm. Two modes are highlighted by the red and green circles at 816 nm and 823 nm, respectively. The 816 nm mode has the highest power and the highest Q-factor, while the 823 nm mode has the highest power extraction efficiency. (b), (c) Normalized $|H_z|$ field distribution inside the cavity at (b) 816 nm and (c) 823 nm.

The cavity modes at 816 nm and 823 nm are primarily constituted out of slab modes with different orientations, as revealed by the spatial Fourier transforms of $|H_z|$ shown in Figs. 3(a) and 3(b), which is the origin of the very differing light extraction efficiencies associated with them. In order to achieve efficient vertical outcoupling into free space, one could apply the so-called band-folding technique [17, 18], by which the photonic crystal lattice is locally modified around the cavity by a superlattice that maps the dominant Fourier components inside the light cone. For example, every second hole can be modified, in which case this method allows for increased vertical outcoupling of cavity modes whose field components have wavevectors $\vec{k}$ that lie close to the edge of the first Brillouin zone. However, vertical outcoupling can be drastically increased if $\vec{k}$ directly coincides with a reciprocal lattice vector $\vec{G}$ of the photonic crystal. This field component can then be directly scattered to the Γ-point at $\vec{k} = 0$ due to Bragg scattering without requiring the bandfolding technique. Our photonic crystal cavity is designed such that the cavity mode at 823 nm has dominant in-plane wave vector components at $\vec{k} = \pm\vec{G}$ (Fig. 3(b)). Therefore, coupling to $\vec{k} = 0$ is possible, resulting in an efficient vertical emission and explaining the mode's reduced Q-factor.

The two major loss mechanisms leading to decay of the cavity mode are radiative emission out of the cavity and absorption by the electrodes. A sufficiently high radiative emission rate ensuring that it is the dominant loss channel is necessary to maintain high extraction efficiencies. This is satisfied by the 823 nm mode. The cavity mode at 816 nm, on the other hand, does not satisfy the condition $\vec{k} = \pm\vec{G}$, which results in a poor extraction efficiency and an increased Q-factor limited by electrode absorption.

One of the reciprocal lattice vectors of the photonic crystal are indicated by a red arrow in Figs. 3(a), 3(b) and the reciprocal lattice points by yellow dots. As can be seen in Fig. 3(b), the dominant k-space components of the 823 nm mode are two

slab modes propagating in opposite directions along the x-direction and forming a standing wave, with wavevectors overlapping with the two reciprocal lattice vectors in the x-direction. As a result, this cavity mode can be Bragg-scattered to the Γ-point and results in vertical emission. On the other hand, the cavity mode at 816 nm features two standing waves. However, these have k-vectors off the high-symmetry points and cannot be coupled to the Γ-point inside the light line, resulting in low extraction efficiency and an irregular far-field pattern.

Fig. 3(c) and 3(d) shows the simulated far field intensity distribution as a function of zenith angle θ and azimuth angle φ. Both far-field patterns are normalized by the maximum intensity at 823 nm. The far field pattern at 823 nm is dominated by the strong vertical emission (at θ = 0°) with very weak side lobes at θ = 30° and φ = 0°/180° (Fig. 3(d)). It has an overlap equal to 98.3% with an ideal 2D Gaussian with an angular 1/e (amplitude) half angle of 11.4°. In contrast, the far field pattern at 816 nm only shows weak emission without preferred directivity (Fig. 3(c)), with most of the power absorbed by the electrodes.

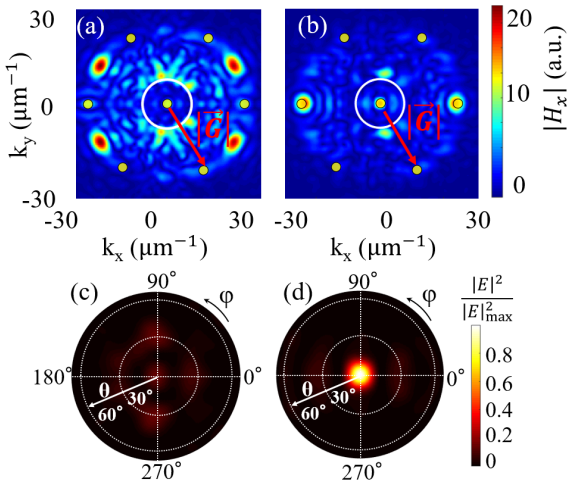

Figure 3. Fourier space distribution of photonic crystal cavity modes at (a) 816 nm and (b) 823 nm. The red arrow indicates a reciprocal lattice vector and the white circle represents the light line. Field components inside the white circle can escape the cavity and emit into free space. Normalized far field emission pattern for (c) 816 nm and (d) 823 nm. Strong vertical emission is expected from the 823 nm mode.

The extraction efficiencies are depicted as a function of the NA in Fig. 4 for the two cavity modes. The bottom mirror is placed 460 nm below the dipole or, equivalently, 350 nm below the bottom surface of the layer stack. In the case of the 823 nm mode, the efficiency increases rapidly and reaches 30% for NA > 0.2 as a result of the highly concentrated vertical emission. The efficiency reaches 50% for NA equal to 0.60 (θ = 37°), which means that single photons emitted by the OAQD have a 50% chance to be emitted in a radiation cone with a half-angle of 37° from the z-direction. Taking all emission outside of the chip into account (NA = 1), the extraction efficiency reaches above 60%. As a comparison, the extraction efficiency from the 816 nm mode is also displayed by the red curve and can be seen to be much lower.

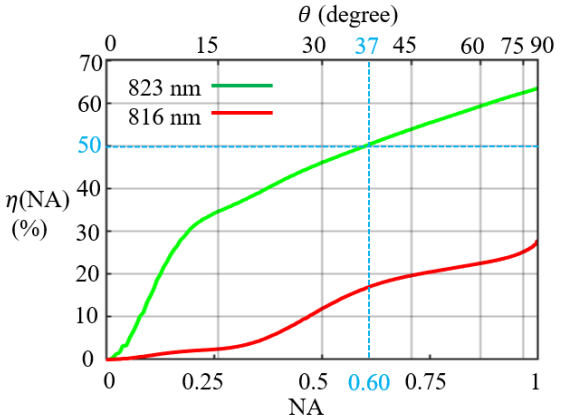

Figure 4. Extraction efficiency η as a function of NA for cavity modes at 816 nm (red) and 823 nm (green). An efficiency above 50% can be achieved for NA > 0.6 for 823 nm.

In order to study how the efficiency and far field pattern are affected by the mirror position, we sweep the mirror-to-OAQD distance from 420 nm to 560 nm with a step size of 20 nm. Fig. 5(a) shows the recorded efficiencies as a function of mirror position for NA equal to 0.3 (green), 0.6 (red), and 0.9 (blue). We observe an optimal mirror position at a distance of 460 nm (mirror position A) with an efficiency of 63.5% for NA = 0.9. The far field emission pattern for this mirror distance is shown in Fig. 5(b). It features a strong vertical emission with very weak side lobes at $\theta = 0°$ and $\varphi = 0°/180°$.

As the mirror position is moved from the optimum (position A), the efficiency does not decrease monotonically. A second efficiency peak is observed at a mirror distance of 520 nm (position B). This can be explained by enhanced sidelobe emission, which is suppressed at position A, and corresponds to the constructive reflection condition for the corresponding sidelobe k-vector. However, the condition for constructive interference is not satisfied any longer for the vertically emitted main lobe, resulting in a reduced efficiency and a non-Gaussian far field emission pattern (Fig. 5(c)).

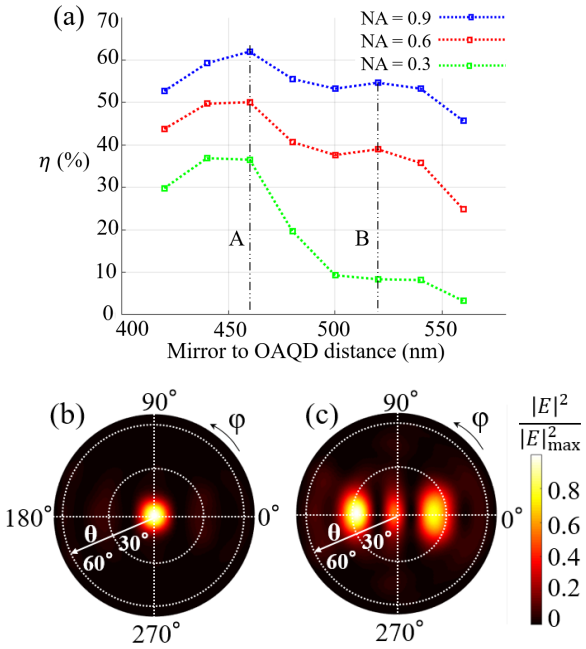

Figure 5. (a) Extraction efficiency η as a function of mirror to OAQD distance for different NA at 823 nm. Normalized far-field emission pattern for a distance equal to (b) 460 nm and (c) 520 nm. The two far-field patterns are independently normalized.

4. EXPERIMENTAL PROGRESS

The fabrication of this structure is also under progress. Fig. 6 shows two SEM micrographs of a first test sample fabricated in a doped AlGaAs/GaAs membrane as presented in Fig. 1(b). A photonic crystal H4 cavity is etched in the 220 nm membrane with a lattice constant of 282 nm and a hole radius of 96 nm. Ti/Au gates are patterned on both the top and bottom membrane surfaces to define the GDQD and OAQD. The bottom gates and top gates have thicknesses of 25 nm (5 nm Ti + 20 nm Au) and 9 nm (2 nm Ti + 7 nm Au), respectively. As seen in Fig. 6(a), the wires are carefully routed between the etched air holes. The geometry of the gates is slightly different than the design presented in Fig.1, but they have the same working principle.

For the fabrication of the devices, a high alignment accuracy is needed between the photonic crystal and the metallic wires. Metallic markers are fabricated by deposition of Ti (5 nm) and Au (80 nm) in a lift-off process after patterning of a 200 nm thick resist (AR-P 6200) with electron beam lithography (EBL). These high-definition markers are used to accurately overlay the metallic wires and the photonic crystal in three consecutive EBL steps. First, the metallic wires (5 nm Ti + 20 nm Au) corresponding to the bottom gates (Fig. 6(b)) are fabricated in the same fashion as the markers, with EBL applied to an 80 nm thick resist and a lift-off process. After the sample is flipped and bonded to a Si substrate with epoxy, the GaAs substrate is completely etched away to access the other side of the heterostructure. Although the metallic markers are now underneath the resulting 220 nm membrane, they can still be recognized by the electron beam writer. Second, the top gates (2 nm Ti + 7 nm Au) are fabricated in the same manner as the bottom gates. Third, the holes are patterned in a

600 nm thick resist by a last EBL step and transferred to the sample by inductively-coupled plasma reactive ion etching with a mixture of Cl_2 and Ar. As a further optimization of the sample quality, BCl_3 or N_2 can be added to the previous gases to reduce the oxidation of aluminum [28].

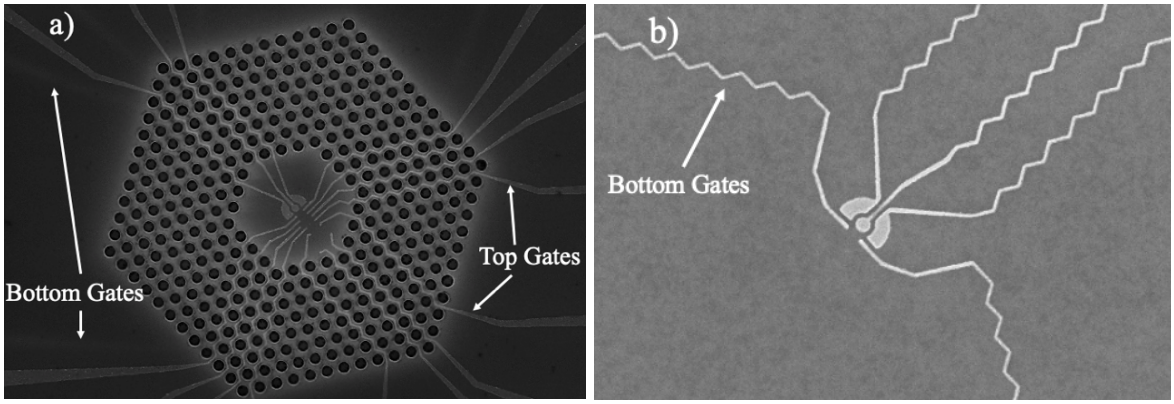

Figure 6. Two SEM images of a 220 nm thick AlGaAs/GaAs test sample with top and bottom metal gates. (a) The top surface of the fabricated structure. The photonic crystal has a lattice constant of 282 nm and a hole radius of 96 nm. The electrode structure is slightly different from that presented in Fig. 1, but follows the same principle of operation. Ti/Au metal wires with a thickness of 9 nm and a width of 30 nm are routed between etched air holes. The bottom gates remain visible through the 220 nm membrane. (b) The bottom surface of the fabricated structure before the membrane is flipped and epoxy bonded to an Si substrate. The bottom gates have a thickness of 25 nm for better visibility after the flip-chip attachment process.

5. CONCLUSION AND REMARKS

We present and numerically analyze an efficient interface between a photonic qubit and a singlet-triplet solid-state spin qubit. The structure is realized by pattering a modified H4 cavity around an OAQD. Instead of using an SAQD as an exciton trap, as proposed in the original quantum state transfer protocol, we use an OAQD since it can be seamlessly integrated and lithographically defined together with the GDQD. The photonic crystal cavity is designed such that the dominant wavevectors of the cavity mode at the OAQD wavelength match the photonic crystal's reciprocal lattice vectors. This enables efficient coupling between the cavity mode and a free space Gaussian beam. In order to further increase the efficiency and shape the far-field emission pattern, a back-reflector is placed below the structure. As a result, we obtain vertical emission with an efficiency greater than 50% if collection optics with NA>0.6 are used. Moreover, the far field emission pattern has an overlap up to 98.3% with an ideal Gaussian beam.

Fabrication and testing of this optical qubit interface are under progress. An electron conveyer belt, which is able to transfer single electrons between adjacent GDQDs, is also being integrated into our design [29, 30].

6. ACKNOWLEDGEMENT

Funded by the Deutsche Forschungsgemeinschaft (DFG, German Research Foundation) under Germany's Excellence Strategy – Cluster of Excellence Matter and Light for Quantum Computing (ML4Q) EXC 2004/1 – 390534769.

We would like to thank Chao Zhao for growing the wafer.

REFERENCES

[1] Elzerman, J. M., et al., "Few-electron quantum dot circuit with integrated charge read out," *Phys. Rev. B* 67, 161308(R) (2003).
[2] Cerfontaine, P., et al., "High-fidelity single-qubit gates for two-electron spin qubits in GaAs," *Phys. Rev. Lett.* 113, 150501 (2014).
[3] Cerfontaine, P., et al., "Closed-loop control of a GaAs-based singlet-triplet spin qubit with 99.5% gate fidelity and low leakage," *Nat. Comm.* 11, 4144 (2020).

[4] Fujita, T., et al., “Nondestructive Real-Time Measurement of a Charge and Spin Dynamics of Photoelectrons in a Double Quantum Dot,” *Phys. Rev. Lett.* 110, 266803 (2013).
[5] Fujita, T., el al., “Single photoelectron spin detection and angular momentum transfer in a gate defined quantum dot,” arXiv:1504.03696 (2015).
[6] Kosaka H., et al., “Coherent Transfer of Light Polarization to Electron Spins in a Semiconductor,” *Phys. Rev. Lett.* 100, 096602 (2008).
[7] Kuwahara, M., et al., “Single charge detection of an electron created by a photon in a g-factor engineered quantum dot,” *Appl. Phys. Lett.* 96, 163107 (2010).
[8] Joecker, B., et al., “Transfer of a quantum state from a photonic qubit to a gate-defined quantum dot,” *Phys. Rev. B* 99, 205415 (2019).
[9] Barnes, W. L., Björk, G., Gérard, J. M., Jonsson, P., Wasey, J. A. E., et al., “Solid-state single photon sources: light collection strategies,” *Eur. Phys. J. D* 18, 197 (2002).
[10] Ding, X., et al., “On-demand single photons with high extraction efficiency and near-unity indistinguishability from a resonantly driven quantum dot in a micropillar,” *Phys. Rev. Lett.* 116, 020401 (2016).
[11] Claudon, J., et al., “A highly efficient single-photon source based on a quantum dot in a photonic nanowire,” *Nat. Photon.* 4, 174 (2010).
[12] Schlehahn, A., et al., “Single-photon emission at a rate of 143 MHz from a deterministic quantum-dot microlens triggered by a mode-locked external-cavity surface-emitting laser,” *Appl. Phys. Lett.* 107, 041105 (2015).
[13] Fischbach, S., et al., “Efficient single-photon source based on a deterministically single quantum dot-microstructure with back side gold mirror,” *Appl. Phys. Lett.* 111, 011106 (2017).
[14] Engle, H.-A., et al., “Quantum optical interface for gate-controlled spintronic devices,” arXiv:cond-mat/0612700 (2006).
[15] Schinner, G. J., et al., “Confinement and interaction of single indirect excitons in a voltage-controlled trap formed inside double InGaAs quantum wells,” *Phys. Rev. Lett.* 110, 127403 (2013).
[16] Purcell, E. M., “Spontaneous emission probabilities at radio frequencies,” *Phys. Rev.* 69, 681 (1946).
[17] Tran, N.-V.-Q., et al., “Vertical high emission in photonic crystal nanocavities by band-folding design,” *Phys. Rev. B* 82, 075120 (2010).
[18] Tran, N.-V.-Q., et al., “Directive emission from High-Q photonic crystal cavities through band folding,” *Phys. Rev. B* 79, 041101(R) (2009).
[19] Yoshie, T., Scherer, A., Hendrickson, J., Khitrova, G., Gibbs, H. M., Rupper, G., Ell, C., Shchekin, O. B., Deppe, D. G., “Vacuum Rabi splitting with a single quantum dot in a photonic crystal cavity,” *Nat.* 432, 200 (2004).
[20] Tajiri, T., et al., “Fabrication and optical characterization of photonic crystal nanocavities with electrodes for gate-defined quantum dots,” *Jpn. J. Appl. Phys*. 59, SGGI05 (2020).
[21] Wu, K., et al., “High-efficiency gate-defined quantum dot to single mode fiber interface assisted by a photonic crystal cavity,” *AIP Adv.* 10, 115016 (2020).
[22] Romero-García, S., Merget, F., Zhong, F., Finkelstein, H., Witzens, J., “Silicon nitride CMOS-compatible platform for integrated photonics applications at visible wavelengths,” *Opt. Expr.* 21, 14036 (2013).
[23] Romero-García, S., Merget, F., Zhong, F., Finkelstein, H., Witzens, J., “Visible wavelength silicon nitride focusing grating coupler with AlCu/TiN reflector,” *Opt. Lett.* 38, 2521 (2013).
[24] Petta, J. R., et al., “Coherent Manipulation of Coupled Electron Spins in Semiconductor Quantum Dots,” *Science* 309, 2180 (2005).
[25] Field, M., et al., “Measurements of Coulomb Blockade with a Noninvasive Voltage Probe,” *Phys. Rev. Lett.* 70, 1311 (1993).
[26] Johnson, A. C., et al., “Singlet-triplet spin blockade and charge sensing in a few-electron double quantum dot,” *Phys. Rev. B* 72, 165308 (2005).
[27] Reilly, D. J., et al., “Fast single charge sensing with a RF quantum point contact,” *Appl. Phys. Lett.* 91, 89 (2007).
[28] Zhou, X., Kulkova, I., Lund-Hansen, T., Lindskov Hansen, S., Lodahl, P., Midolo, L., “High-efficiency shallow-etched grating on GaAs membranes for quantum photonic applications,” *Appl. Phys. Lett.* 113, 251103 (2018).
[29] Seidler, I., Struck, T., Xue, R., Focke, N., Trellenkamp, S., Bluhm, H., Schreiber, L. R., “Conveyor-mode single-electron shuttling in Si/SiGe for a scalable quantum computing architecture,” arXiv:2108.00879 (2021).
[30] Laucht, A., et al., “Roadmap on quantum nanotechnologies,” *Nanotechnol.* 32, 162003 (2021).